

Magnetoinfrared spectroscopic study of thin Bi₂Te₃ single crystals

L.-C. Tung,¹ W. Yu,² P. Cadden-Zimansky,³ I. Miotkowski,⁴ Y. P. Chen,⁴ D. Smirnov,¹ and Z. Jiang²

¹*National High Magnetic Field Laboratory, Tallahassee, Florida 32310, USA*

²*School of Physics, Georgia Institute of Technology, Atlanta, Georgia 30332, USA*

³*Physics Program, Bard College, Annandale-on-Hudson, New York 12504, USA*

⁴*Department of Physics, Purdue University, West Lafayette, Indiana 47907, USA*

(Received 17 August 2015; revised manuscript received 24 January 2016; published 29 February 2016)

Thin Bi₂Te₃ single crystals laid on Scotch tape are investigated by Fourier transform infrared spectroscopy at 4 K and in a magnetic field up to 35 T. The magnetotransmittance spectra of the Bi₂Te₃/tape composite are analyzed as a stacked-slab system, and the average thickness of Bi₂Te₃ is estimated to be $6.4 \pm 1.7 \mu\text{m}$. The optical conductivity of Bi₂Te₃ at different magnetic fields is then extracted, and we find that the magnetic field modifies the optical conductivity in the following ways: (1) Field-induced transfer of the optical weight from the lower-frequency regime ($< 250 \text{ cm}^{-1}$) to the higher-frequency regime ($> 250 \text{ cm}^{-1}$) due to the redistribution of charge carriers across the Fermi surface. (2) Evolving of a Fano-resonance-like spectral feature from an antiresonance to a resonance with increasing magnetic field. Such behavior can be attributed to the electron-phonon interactions between the E_u^1 optical phonon mode and the continuum of electronic transitions. (3) Cyclotron resonance resulting from the intervalence band Landau level transitions, which can be described by the electrodynamics of massive Dirac holes.

DOI: [10.1103/PhysRevB.93.085140](https://doi.org/10.1103/PhysRevB.93.085140)

Recently, bismuth telluride (Bi₂Te₃), along with Bi₂Se₃, Sb₂Te₃, and other V₂VI₃ binary alloys, were discovered to be a physical realization of a three-dimensional (3D) topological insulator (TI) [1]. The insulating bulk of a TI is enclosed by a robust conducting surface, which exhibits a linear Dirac-like band structure protected by time-reversal symmetry. The strong spin-orbit coupling in TIs also leads to unusual spin-momentum locking [2] as well as unique magnetoelectric effects [3]. These phenomena may have profound implications in future nanoelectronic, spintronic, and thermoelectric devices [4–6]. More TIs are discovered and/or proposed, including the SrTiO₃/LaAlO₃ interface [7,8], InAs/GaSb coupled quantum wells [9], HgTe under strain [10], gray tin [11], and topological oxides [12–14].

Since its discovery, considerable efforts have been made to understand the electronic properties of both surface and bulk charge carriers in 3D TIs. These properties can be studied via optical techniques including angle-resolved photoemission spectroscopy, optical conductivity, and magnetoinfrared spectroscopy. The optical conductivity and cyclotron resonance (CR) of several TI materials have been reported [15–24]. In particular, transitions between the quantized Landau levels (LLs) of the Dirac surface states have been observed in Bi_{0.91}Sb_{0.09}, though it seems to suggest three distinct Fermi velocities, thus implying three Dirac cones on the [211] surface [19]. In Bi₂Se₃, interband LL transitions have also been observed, and they can be attributed to the electrodynamics of massive Dirac fermions in TIs [24]. In this paper, magnetoinfrared transmittance spectroscopy is used to obtain the optical conductivity of thin Bi₂Te₃ single-crystal flakes laid on a strip of Scotch tape. The thickness of the Bi₂Te₃ is reduced by exfoliation in order to suppress the bulk contribution and allow for appreciable infrared transmission. Transmittance spectroscopy is preferred for resolving optical modes in TIs, because an optical mode generally results in an absorption dip in the transmittance spectrum. Our measurements reveal that a Fano resonance [25] occurs at the E_u^1 optical phonon

mode [26,27], which evolves from an antiresonance (enhanced transmission) to a resonance (absorption) with increasing magnetic field. In addition, a broad magnetic-field-dependent absorption is observed due to the intervalence band LL transitions of massive Dirac holes [22,24,28,29].

Bi₂Te₃ crystallizes in a rhombohedral structure (point group $\bar{3}mD_3d$) with quintuple layers stacked along the trigonal c axis [30]. The neighboring quintuple layers are bounded by weak van der Waals forces, allowing for exfoliation of Bi₂Te₃ thin layers. In this work, we first exfoliate a thin Bi₂Te₃ crystal from a larger piece and lay it on a strip of Scotch tape. The thickness of this thin crystal is further reduced by repeatedly lifting layers from it. Optical microscopy investigation reveals that the resulting sample consists of thousands of thin flakes with most of them exhibiting an area of 100–300 μm^2 . The Bi₂Te₃/tape composite is then placed in a liquid helium cryostat held at 4 K subject to a high magnetic field up to 35 T. Magnetoinfrared transmission spectra are measured by a Fourier transform infrared spectrometer using light pipe optics, and the transmittance is obtained by the ratio to a reference spectrum taken in the absence of the sample.

A set of magnetotransmittance spectra of the Bi₂Te₃/tape composite at different magnetic fields is shown in Fig. 1(b) and compared with that of the tape at zero field in Fig. 1(a). Here, as one can see, the Bi₂Te₃/tape composite is transparent at low frequencies, while the transmittance drops rapidly, approaching 1200 cm^{-1} (1 eV \simeq 8065 cm^{-1}), as indicated by the (blue) arrow in Fig. 1(b). This drop in transmittance occurs in all the spectra taken at different magnetic fields, and it can be attributed to the rise of the conductance/absorption due to the electronic transitions from the valence to conduction band. The drop-off frequency ($\sim 1200 \text{ cm}^{-1}$) implies a band gap around 0.15 eV, consistent with that reported in literature [31,32]. The parallel surfaces of the tape and the Bi₂Te₃ flakes cause a series of etalon oscillations. The period of the oscillation depends on the magnetic field owing to the field-dependent refractive index of Bi₂Te₃. Nevertheless, a discernible dip located at

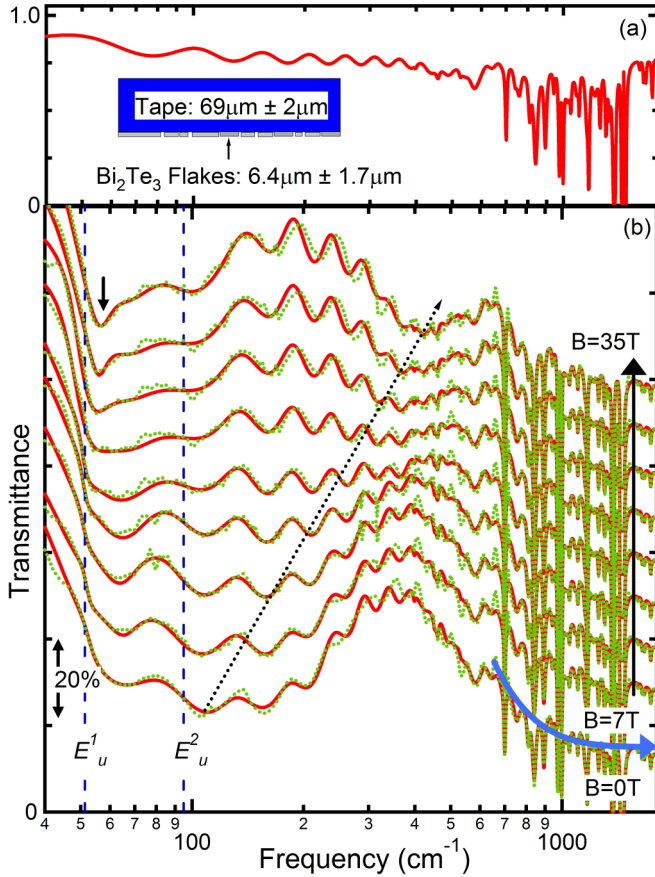


FIG. 1. (a) The transmittance spectrum of the Scotch tape. The tape is transparent at low frequencies ($< 700 \text{ cm}^{-1}$), while sharp absorption lines appear at $> 700 \text{ cm}^{-1}$. These sharp lines have minimal effects to the spectral features discussed in this work, as those features are much broader and occur at lower frequencies. Inset: The schematic layout of the Bi₂Te₃ flakes on Scotch tape. (b) The magnetotransmittance spectra (green) of the Bi₂Te₃/tape composite. The spectra are shown every 4 T from 7 T to 35 T and each spectrum is offset vertically for clarity. Red solid lines represent the best fits to the data via modeling the composite as a stacked-slab system and considering parallel interface interference. The (blue) arrow approaching 1200 cm^{-1} indicates where the transmittance drops rapidly with increasing photon frequency. The short arrow around 50 cm^{-1} labels the spectral feature that can be attributed to a Fano resonance. A broad dip gradually shifts to higher frequencies with increasing magnetic field, as indicated by the dotted arrow. The infrared-active optical phonon modes are marked with (blue) dashed lines with the values taken from Ref. [26].

around 50 cm^{-1} [as indicated by the short arrow in Fig. 1(b)] develops at high magnetic fields, while another broader dip gradually blueshifts to higher frequencies as guided by the dotted arrow.

To extract the optical conductivity of Bi₂Te₃, the acquired spectra of the Bi₂Te₃/tape composite are modeled as a stacked-slab system considering the etalon oscillations due to the parallel interfaces of each slab using RefFit [33]. The dielectric function of each layer is modeled by a set of Drude-Lorentz modes as $\epsilon_1(\omega) + i\epsilon_2(\omega) = \epsilon_\infty + \sum_j \frac{\omega_{pj}^2}{\omega_{0j}^2 - \omega^2 - i\gamma_j\omega}$, where ϵ_∞ is the high-frequency dielectric constant. The parameters

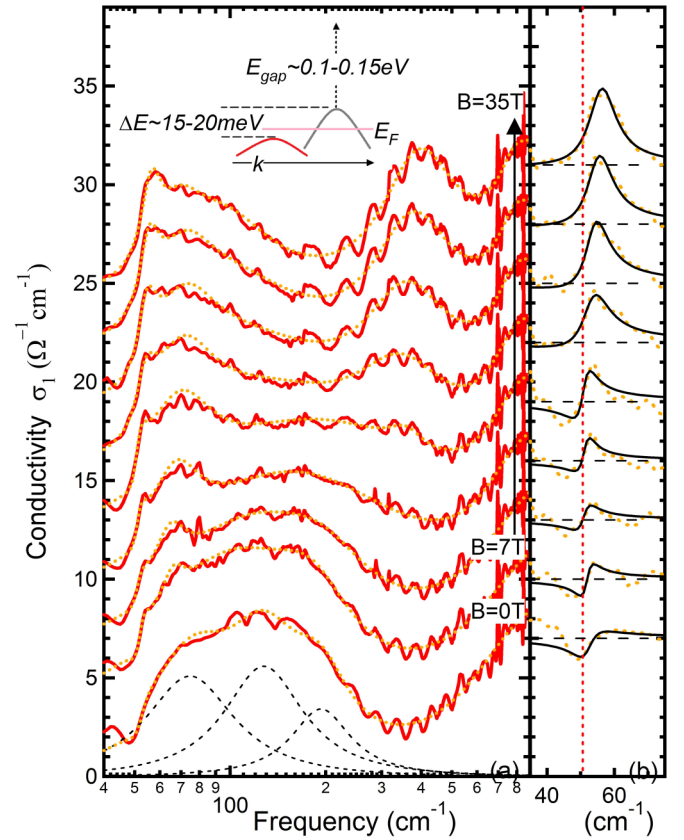


FIG. 2. (a) The real part of the optical conductivity of Bi₂Te₃. The spectra are shown in every 4 T from 7 T to 35 T and each spectrum is offset vertically for clarity. The (orange) dashed lines represent the as-calculated optical conductivity from the best fits to the data, and the (red) solid lines represent the corrected optical conductivity, which considers the differences between the best fits and the measured transmittance spectra in Fig. 1(b). Three Lorentzian modes, shown in (black) dashed lines, are used to describe the broad spectral feature centered at $\sim 150 \text{ cm}^{-1}$. Inset: Schematic band structure of Bi₂Te₃ reproduced from Ref. [32]. (b) The Fano resonance is separated for further analysis. The solid lines represent the best fits to the data using a Fano formula.

ω_{pj}, ω_{0j} , and γ_j are the plasma frequency, the oscillator's natural frequency, and the linewidth of the j th Lorentz oscillator, respectively. The real part of the optical conductivity can then be calculated by $\sigma_1 = \frac{\omega\epsilon_2}{4\pi}$. It is important to note that the net transmittance spectra of the Bi₂Te₃ flakes cannot be directly obtained by the ratio of the transmittance spectra of the Bi₂Te₃/tape composite to that of the tape, because the tape-vacuum and tape-Bi₂Te₃ interfaces have very different Fresnel coefficients. The best fits to the data are shown in Fig. 1(b) for each magnetic field. An asymmetric, Fano-resonance-like spectral feature is revealed at low frequencies near the infrared-active E_u^1 optical phonon mode, which will be discussed below in the context of Fig. 2(b).

From the transmittance spectrum of the tape [Fig. 1(a)], the dielectric function and the thickness of the tape can be determined from the etalon oscillations. These parameters are held constant when analyzing the magnetotransmittance spectra of the Bi₂Te₃/tape composite, and the best fits to the

data in Fig. 1(b) (red solid lines) are obtained using $69 \pm 2 \mu\text{m}$ for the thickness of the tape and $6.4 \pm 1.7 \mu\text{m}$ as the average thickness of Bi_2Te_3 flakes. For the sake of simplicity, in this work we regard the flakes as a uniform thin slab, disregarding the existence of the surface layers. The optical conductivity of Bi_2Te_3 can then be calculated from the best fit of the magnetotransmittance spectrum.

The optical conductivity spectra of Bi_2Te_3 at selected fields are plotted in Fig. 2(a). To ensure that minute or non-Lorentzian conductivity contributions are not neglected by modeling, the difference between the fits and the measured transmittance spectra in Fig. 1(b) are calculated, and a correction is applied to the as-calculated conductivity spectra by adding a conductivity correction $\Delta\sigma_1 = \frac{n_1 c}{4\pi\mu_1} \Delta\alpha \simeq \frac{n_1 c}{4\pi\mu_1 d} \frac{\Delta T}{T}$, where μ_1 is the magnetic permeability which is assumed to be 1 for nonmagnetic materials, n_1 is the real part of the refractive index which is obtained from the dielectric function, d is the average thickness of the flakes, c is the speed of light, and $\Delta\alpha$ represents a correction to the absorption coefficient, which amounts to the observed transmittance difference. In Fig. 2(a), we plot the corrected conductivity spectra overlaid on top of the as-calculated spectra for comparison. It is clear that the model did not completely remove the etalon oscillations due to its oversimplicity. Nevertheless, the period of the oscillations in the corrected conductivity spectra agrees with the thickness of the tape, extracted from Fig. 1(a).

At low magnetic fields, a broad conductivity peak [modeled as three Lorentzian modes in Fig. 2(a)] is evidenced at $\sim 150 \text{ cm}^{-1}$. We notice that a double-Lorentzian spectral structure around 200 cm^{-1} was previously observed in $\text{Bi}_2\text{Te}_2\text{Se}$ and attributed to the transitions from the impurity states to the electronic continuum states [20]. In this study, Bi_2Te_3 is p -doped [34] and the center of this broad peak coincides with the band offset between the upper and the lower valence bands [32]. Therefore, we attribute it to the continuum of the electronic transitions from the lower valence band to the empty states above the Fermi surface in the upper valence band.

The conductivity mode located at $\sim 50 \text{ cm}^{-1}$ invokes the asymmetric line shape of a Fano resonance [25] and consistently evolves from an antiresonance (a dip) to a resonance (a peak) with increasing magnetic field, as shown in Fig. 2(b). Fano resonance is ubiquitous across several branches of physics, and it describes the quantum interference between two coupled transition pathways: one via a discrete excited state and the other via a continuum of states. In this study, the discrete state is the E_u^1 optical phonon mode [26,27], while the continuum of states consists of the transitions from the lower valence band to the empty states in the upper valence band. In the presence of an applied magnetic field, the intervalence band transitions are dominated by the quasicontinuous Landau level transitions with linewidth larger than 70 cm^{-1} . The optical phonon mode and the continuum of the electronic transitions are coupled via strong electron-phonon interactions, which can be attributed to the ‘‘charged-phonon theory’’[35,36] and/or the topological magnetoelectric effect [18]. A magnetic-field tunable Fano resonance was also found in Bi_2Se_3 ($\sim 64 \text{ cm}^{-1}$; α -phonon mode) and attributed to the topological magnetoelectric and magnetostriction effects [18]. Various types of Fano resonance resulting from the coupling between the

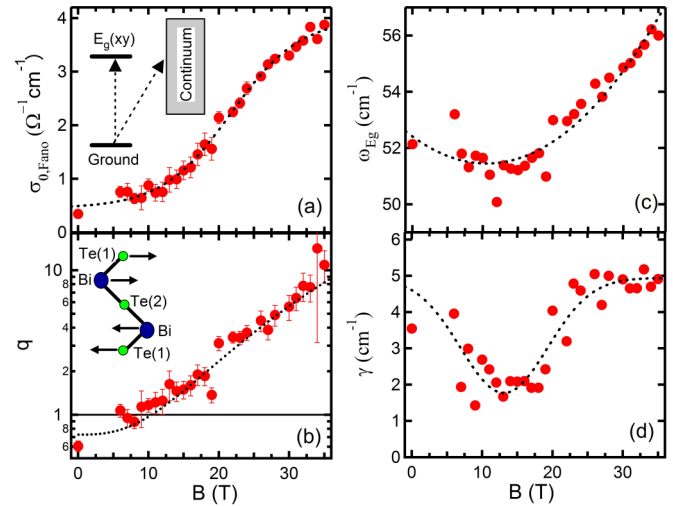


FIG. 3. (a) $\sigma_{0,Fano}$ as a function of the magnetic field. Inset: Schematic energy-level diagram of the Fano resonance. (b) The dimensionless Fano parameter q as a function of the magnetic field. Inset: The displacement of ions of the E_u^1 phonon mode. (c) The energy of the optical phonon mode E_u^1 as a function of the magnetic field. (d) The linewidth of the Fano resonance γ as a function of the magnetic field. The dotted lines are drawn as guides for the magnetic-field dependence; they do not result from a theoretical model.

optical phonon modes and electronic transitions were observed in $\text{Bi}_2\text{Se}_2\text{Te}$ and graphitic materials [20,36].

To separate the optical conductivity of the Fano resonance for quantitative analysis, other Lorentzian modes are removed and the contribution of the Fano resonance is isolated and plotted in Fig. 2(b). The conductivity of a Fano resonance can be described by $\Delta\sigma_{Fano} = \sigma_{0,Fano} \frac{q^2 + 2qz - 1}{q^2(1+z^2)}$, with $z = \frac{\omega - \omega_{Eu}}{\gamma}$ and $\sigma_{0,Fano} = \frac{\omega_p^2}{4\pi\gamma}$, where ω_p is the plasma frequency, ω_{Eu} is the phonon energy, γ is the linewidth, and q is the dimensionless Fano parameter which characterizes the resonance line shape. When $|q| \ll 1$, the Fano effect results in an antiresonance with asymmetric line shape. When $|q| \gg 1$, it becomes a resonance and its line shape can be well approximated by a Lorentzian mode.

As shown in Fig. 2(b), the low-frequency conductivity contribution can be well fitted by the asymmetric line shape of a Fano resonance. The fitting parameters at different magnetic fields are plotted in Fig. 3. In Fig. 3(b), the Fano parameter q gradually increases from $q < 1$ to $q \gg 1$ with increasing magnetic field crossing over $q \simeq 1$ at around $B \simeq 10 \text{ T}$. Similarly, the optical strength $\sigma_{0,Fano}$ of the Fano resonance and the E_u^1 phonon energy start to rise at the crossover field as shown in Figs. 3(a) and 3(c), respectively. The linewidth γ appears to find a minimum at $B \simeq 10 \text{ T}$, as shown in Fig. 3(d).

The observed Fano resonance, as well as that reported in Bi_2Se_3 , is unusual, because the magnetic-field-induced modification of the Fano effect is rarely found in nonmagnetic systems [18]. In addition, it involves an interaction that couples a lattice excitation (an optical phonon mode) and the electronic transitions between the valence bands. The electron-phonon interactions between the α -phonon mode and the electronic

transitions in Bi_2Se_3 were attributed to the magnetostriction in the system with enhanced spin-orbit coupling and the magnetoelectric coupling in a nontrivial TI [18]. A local electric field, induced by the applied magnetic field via the magnetoelectric effect [37], modifies the motion of the Bi ions and thus the optical phonon mode [18]. In Bi_2Se_3 , the Fano resonance is observed when the magnetic field is applied in the direction parallel to the displacement of the Bi ions in the α -phonon mode [18], whereas in Bi_2Te_3 , it is observed near the E_u^1 optical phonon mode in which the displacement of the Bi ions are perpendicular to the magnetic-field direction [26,27], as shown in the inset to Fig. 3(b).

The observed Fano-resonance-like behavior is also consistent with the ‘‘charged phonon theory’’[35,36], in which the optical phonon mode ‘‘borrows’’ optical strength (charges) from the electronic transitions or vice versa, depending on the relative energies of the electronic and the optical transitions. This theory has been successfully adopted to explain the Fano effect in graphitic materials [36]. In our case, the electronic transitions gradually shift to higher energies due to the diamagnetic shift of the Fermi level, and at $B \simeq 10$ T it reaches the energy of the E_u^1 phonon mode. For $B > 10$ T, the optical phonon mode borrows the charges from the electronic transitions, thus resulting in the rise of the optical strength and the antiresonance-to-resonance crossover. The crossover field is consistent with the expected diamagnetic shift of the Fermi level with a hole mass equal to $0.08m_e$ [31], where m_e is the free electron mass.

Other than the Fano resonance, the applied magnetic field gradually transfers the optical weight from the broad peak centered at $\simeq 150$ cm^{-1} to higher frequencies. Magnetic field is expected to induce the transitions between quantized LLs between the lower and the upper valence bands. The degeneracy and the separation of the LLs increase with increasing magnetic field, resulting in the observed optical weight transfer and the increase of the transition energy. The magnetic-field-induced effect can be evaluated by subtracting the optical conductivity obtained at $B = 0$ T from that obtained at $B \neq 0$ T: $\Delta\sigma_B = \sigma_B(\omega) - \sigma_{B=0T}(\omega)$. The magnetic-field-induced change in optical conductivity is plotted in Fig. 4(c), where a broad peak develops as the magnetic field increases and the peak gradually shifts to higher frequencies with increasing optical strength (\propto the enclosed area).

The magnetic-field-induced broad peak is analyzed as a CR resulting from LL transitions using $\Delta\sigma_B = \frac{\Delta\sigma_{B0}}{1 + (\frac{\omega - \omega_c}{\gamma})^2}$, where

the amplitude $\Delta\sigma_{B0} = \frac{\omega_p^2}{4\pi\gamma}$ represents the optical strength of the CR, ω_c is the cyclotron frequency, and γ is the linewidth. The cyclotron frequency ω_c and the linewidth γ of the CR are plotted in Fig. 4(a), while the optical strength $\Delta\sigma_{B0}$ is plotted in Fig. 4(b). The optical strength rises with magnetic field due to the increasing LL degeneracy and density of states in a 3D electron system. It is clear that the transition energy does not extrapolate to zero at zero magnetic field, so the observed CR is not a consequence of the intraband LL transitions. Moreover, the energy of the CR falls in the range of several tens of meV, whereas the excitonic interband LL transitions (from the valence to conduction bands) reside in the range of several hundred meV [24]. We notice that the observed transition energy is close to the band offset between the lower and upper

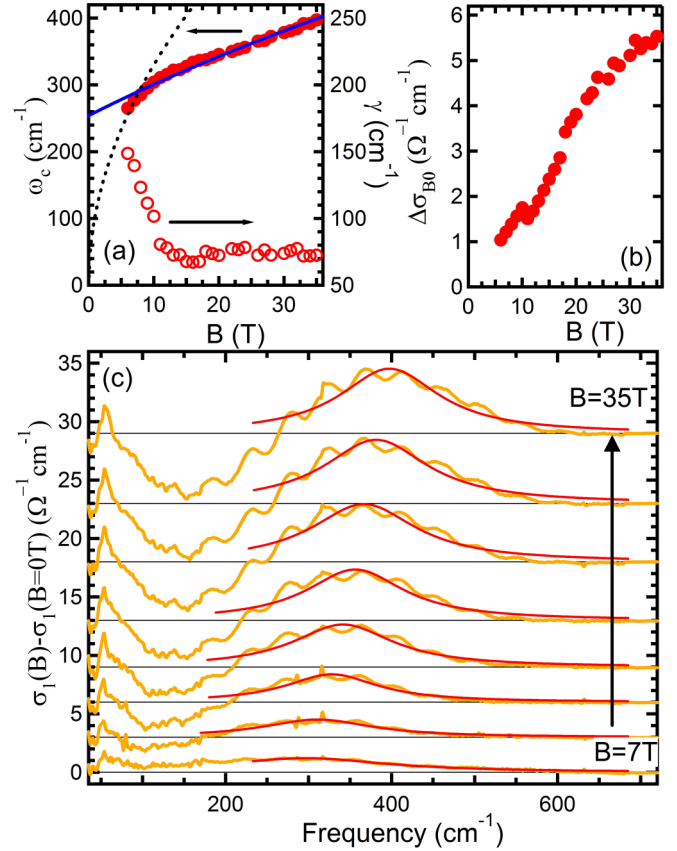


FIG. 4. (a) The transition energy ω_c and the linewidth γ as a function of the magnetic field. The (blue) solid line represents the best fitting curve to Eq. (1). The (black) dashed line represents the transition energy from the $n = 0$ LL to the $n = 1$ LL in the Dirac surface state with a Fermi velocity $v_F \simeq 0.36 \times 10^6$ m/s. (b) The optical strength $\Delta\sigma_{B0}$ as a function of the magnetic field. (c) The magnetic-field-induced optical conductivity change $\Delta\sigma_B$ from 7 T to 35 T with 4 T interval. Each conductivity spectrum is offset vertically for clarity. The horizontal lines label the positions where the change of the optical conductivity is zero and the red solid lines are the Lorentzian fits to the data.

valence bands in Bi_2Te_3 [inset to Fig. 2(a)]. Therefore, the observed magnetic-field-dependent mode can be attributed to the transitions from the LLs in the lower valence band to those in the upper valence band.

Next, we will attempt to quantitatively describe the magnetic-field dependence of ω_c in Fig. 4(a) as an intervalence band LL transition. The holes in the bulk valence bands are described as massive Dirac fermions, and the energies of the LLs of massive Dirac fermions disperse as [28,29]

$$E = \pm \sqrt{\frac{E_g^2}{4} + E_g \left[\frac{\hbar e B}{2m^*} \left(n + \frac{1}{2} \right) \pm \frac{1}{2} g_0 \mu_B B \right]}, \quad (1)$$

where E_g is the energy of the direct band gap, μ_B is the Bohr magneton, m^* is the effective mass of the carriers, n is the LL index, and g_0 is Landé g factor. The first \pm sign indicates the energy of the conduction (+) or the valence (-) band, while the second \pm sign sets the spin state of the LL. For simplification, we assume that the LLs of both valence

bands can be described by Eq. (1), but with different band gap and effective mass, disregarding their relative positions in the Brillouin zone [as shown in the inset to Fig. 2(a)]. We also neglect the spin-flip transitions and set the same g factor for both bands. The transition energy is then insensitive to the choice of the g_0 value. The hole effective mass $m_{h,up}^*$ of the upper valence band is selected to be $0.08m_e$, because this value was also determined by a CR measurement [31]. The band gap of the upper valence band is given as $E_{g,up} \simeq 0.15$ eV [32]. The effective mass $m_{h,low}^*$ and the band gap $E_{g,low}$ of the lower valence band are left as fitting parameters. The transition energy ω_c can then be attributed to the transition from the $n = 1$ LL in the lower valence band to the $n = 0$ LL in the upper valence band. The calculated magnetic-field dependence of the transition energy is plotted in Fig. 4(a) in a blue solid line. From the best fitting curve, the hole effective mass of the lower valence band is found to be $m_{h,low}^* \simeq 0.088m_e$ and the band gap $E_{g,low} \simeq 0.21$ eV. The hole effective mass of the lower valence band is very close to the reported value of $m^* = 0.09m_e$ for the second hole band [31], although the band offset between the valence bands is found to be $\Delta E \simeq 30$ meV from this simple model, larger than $\Delta E \simeq 20$ meV estimated from transport measurements [38]. From these band parameters, one can evaluate the band velocity v_D of the massive Dirac fermions by $v_D = \sqrt{E_g/m^*}$. The band velocities are $v_D \simeq 0.58 \times 10^6$ m/s and $v_D \simeq 0.65 \times 10^6$ m/s for the upper and lower valence bands, respectively. These values are slightly larger than that ($v_D \simeq 0.46 \times 10^6$ m/s) found in Bi_2Se_3 [24].

Transitions between the LLs of the Dirac surface states cannot be distinguished from bulk LL transitions due to the broad linewidth of the CR. However, we notice that the transition energy ω_c deviates from Eq. (1) at $B < 10$ T, while the linewidth becomes substantially broader [Fig. 4(a)].

The dashed line in Fig. 4(a) illustrates the contribution of the $n = 0 \rightarrow 1$ LL transition of the Dirac surface states with a Fermi velocity $v_F \simeq 0.36 \times 10^6$ m/s [39]. It is possible that the CR of the surface carriers indeed contributes to the optical conductivity at low magnetic fields. At a higher field, however, the diamagnetic shift of the Fermi level depletes the carriers in the surface band, and thus the intervalence band LL transitions dominate.

In summary, the optical conductivity of thin Bi_2Te_3 single crystals is studied by magnetoinfrared transmittance spectroscopy in high magnetic fields. An anomalous field-tunable Fano resonance is observed, and it is attributed to the electron-phonon interactions between the E_u^1 optical phonon mode and the continuum of the electronic transitions in the valence bands. The strong electron-phonon interactions might be suggestive of the topological magnetoelectric effect. In addition, a broad absorption mode is found to increase in optical strength and the central energy with increasing magnetic field, and it can be attributed to the transition from the $n = 1$ LL in the lower valence band to the $n = 0$ LL in the upper valence band. The CR of the surface LLs cannot be clearly identified in our measurement, but it might contribute to the unusual broadening of the absorption at lower fields ($B < 10$ T). Further experimental studies are needed on intrinsic TI materials with a truly insulating bulk.

This work is supported by the DOE (Grant No. DE-FG02-07ER46451). The TI crystal synthesis at Purdue University is supported by the DARPA MESO program (Grant No. N66001-11-1-4107). The infrared measurements are carried out at the National High Magnetic Field Laboratory, which is supported by NSF Cooperative Agreement No. DMR-0654118, by the State of Florida, and by the DOE.

-
- [1] For recent reviews, see, for example, M. Z. Hasan and C. L. Kane, *Rev. Mod. Phys.* **82**, 3045 (2010); and X.-L. Qi and S.-C. Zhang, *ibid.* **83**, 1057 (2011).
- [2] D. Hsieh, Y. Xia, D. Qian, L. Wray, J. H. Dil, F. Meier, J. Osterwalder, L. Patthey, J. G. Checkelsky, N. P. Ong, A. V. Fedorov, H. Lin, A. Bansil, D. Grauer, Y. S. Hor, R. J. Cava, and M. Z. Hasan, *Nature (London)* **460**, 1101 (2009).
- [3] W.-K. Tse and A. H. MacDonald, *Phys. Rev. B* **82**, 161104 (2010).
- [4] K. J. Pluciski, W. Gruhn, I. V. Kityk, W. Imioek, H. Kaddouri, and S. Benet, *Opt. Commun.* **204**, 355 (2002).
- [5] L. Fu and C. L. Kane, *Phys. Rev. Lett.* **100**, 096407 (2008).
- [6] J. E. Moore, *Nature (London)* **464**, 194 (2010).
- [7] A. Ohtomo and H. Y. Hwang, *Nature (London)* **427**, 423 (2004).
- [8] N. Reyren, S. Thiel, A. D. Caviglia, L. Fitting Kourkoutis, G. Hammerl, C. Richter, C. W. Schneider, T. Kopp, A.-S. Rüetschi, D. Jaccard, M. Gabay, D. A. Muller, J.-M. Triscone, and J. Mannhart, *Science* **317**, 1196 (2007).
- [9] I. Knez, R. R. Du, and G. Sullivan, *Phys. Rev. B* **81**, 201301(R) (2010).
- [10] C. Bouvier, T. Meunier, P. Ballet, X. Baudry, R. B. G. Kramer, and L. Lévy, [arXiv:1112.2092v1](https://arxiv.org/abs/1112.2092v1).
- [11] L. Fu and C. L. Kane, *Phys. Rev. B* **76**, 045302 (2007).
- [12] A. Shitade, H. Katsura, J. Kuneš, X.-L. Qi, S.-C. Zhang, and N. Nagaosa, *Phys. Rev. Lett.* **102**, 256403 (2009).
- [13] J. Hosub, S. H. Rhim, J. Im, and A. Freeman, *Sci. Rep.* **3**, 1651 (2013).
- [14] B. Yan, M. Jansen, and C. Felser, *Nat. Phys.* **9**, 709 (2013).
- [15] V. A. Kulbachinskii, N. Miura, H. Arimoto, T. Ikaida, P. Lostak, and C. Drasar, *J. Phys. Soc. Jpn.* **68**, 3328 (1999).
- [16] N. P. Stepanov, S. A. Nemov, M. K. Zhitinskaya, and T. E. Svechnikova, *Semiconductors* **41**, 786 (2007).
- [17] N. P. Butch, K. Kirshenbaum, P. Syers, A. B. Sushkov, G. S. Jenkins, H. D. Drew, and J. Paglione, *Phys. Rev. B* **81**, 241301(R) (2010).
- [18] A. D. LaForge, A. Frenzel, B. C. Pursley, T. Lin, X. Liu, J. Shi, and D. N. Basov, *Phys. Rev. B* **81**, 125120 (2010).
- [19] A. A. Schafgans, K. W. Post, A. A. Taskin, Y. Ando, X.-L. Qi, B. C. Chapler, and D. N. Basov, *Phys. Rev. B* **85**, 195440 (2012).
- [20] P. Di Pietro, F. M. Vitucci, D. Nicoletti, L. Baldassarre, P. Calvani, R. Cava, Y. S. Hor, U. Schade, and S. Lupi, *Phys. Rev. B* **86**, 045439 (2012).
- [21] R. Valdes Aguilar, A. V. Stier, W. Liu, L. S. Bilbro, D. K. George, N. Bansal, L. Wu, J. Cerne, A. G. Markelz, S. Oh, and N. P. Armitage, *Phys. Rev. Lett.* **108**, 087403 (2012).

- [22] B. C. Chapler, K. W. Post, A. R. Richardella, J. S. Lee, J. Tao, N. Samarth, and D. N. Basov, *Phys. Rev. B* **89**, 235308 (2014).
- [23] L. Wu, W.-K. Tse, M. Brahlek, C. M. Morris, R. V. Aguilar, N. Koirala, S. Oh, and N. P. Armitage, *Phys. Rev. Lett.* **115**, 217602 (2015).
- [24] M. Orlita, B. A. Piot, G. Martinez, N. K. Sampath Kumar, C. Faugeras, M. Potemski, C. Michel, E. M. Hankiewicz, T. Brauner, C. Drasar, S. Schreyeck, S. Grauer, K. Brunner, C. Gould, C. Brune, and L. W. Molenkamp, *Phys. Rev. Lett.* **114**, 186401 (2015).
- [25] U. Fano, *Phys. Rev.* **124**, 1866 (1961).
- [26] C. R. Richter, W. Kohler, and H. Becker, *Phys. Status Solidi B* **84**, 619 (1977).
- [27] W. Kullmann, J. Geurts, W. Richter, H. Rauh, U. Steigenbrger, G. Eichhorn, and R. Geick, *Phys. Status Solidi B* **125**, 131 (1984).
- [28] P. A. Wolff, *J. Phys. Chem. Solids* **25**, 1057 (1964).
- [29] E. D. Palik and J. K. Furdyna, *Rep. Prog. Phys.* **33**, 1193 (1970).
- [30] E. M. Black, L. Conwell, L. Seigle, and C. vW. Spencer, *J. Phys. Chem. Solids* **2**, 240 (1957).
- [31] Bismuth telluride (Bi_2Te_3) effective masses, in *Non-Tetrahedrally Bonded Elements and Binary Compounds I*, Landolt-Bornstein-Group III Condensed Matter Vol. 41C, edited by O. Madelung, U. Rössler, and M. Schulz (Springer, Berlin, 1998).
- [32] V. A. Kulbachinskii, M. Inoue, M. Sasaki, H. Negishi, W. X. Gao, K. Takase, Y. Gimán, P. Lostak, and J. Horak, *Phys. Rev. B* **50**, 16921 (1994).
- [33] A. B. Kuzmenko, *Rev. Sci. Instrum.* **76**, 083108 (2005).
- [34] M. Hajlaoui, E. Papalazarou, J. Mauchain, L. Perfetti, A. Taleb-Ibrahimi, F. Navarin, M. Monteverde, P. Auban-Senzier, C. R. Pasquier, N. Moisan, D. Boschetto, M. Neupane, M. Z. Hasan, T. Durakiewicz, Z. Jiang, Y. Xu, I. Miotkowski, Y. P. Chen, S. Jia, H. W. Ji, R. J. Cava, and M. Marsi, *Nat. Commun.* **5**, 3003 (2014).
- [35] M. J. Rice and H.-Y. Choi, *Phys. Rev. B* **45**, 10173 (1992).
- [36] E. Cappelluti, L. Benfatto, M. Manzardo, and A. B. Kuzmenko, *Phys. Rev. B* **86**, 115439 (2012).
- [37] A. M. Essin, J. E. Moore, and D. Vanderbilt, *Phys. Rev. Lett.* **102**, 146805 (2009).
- [38] H. Kohler, *Phys. Status Solidi B* **74**, 591 (1976).
- [39] M. Hajlaoui, E. Papalazarou, J. Mauchain, G. Lantz, N. Moisan, D. Boschetto, Z. Jiang, I. Miotkowski, Y. P. Chen, A. Taleb-Ibrahimi, L. Perfetti, and M. Marsi, *Nano Lett.* **12**, 3532 (2012).